Design and characterization of 2D MXene-based electrode with high-rate capability

Wang, Xuehang; Bannenberg, Lars

DOI
10.1557/s43577-021-00150-z

Publication date
2021

Document Version
Final published version

Published in
MRS Bulletin

Design and characterization of 2D MXene-based electrode with high-rate capability

Xuehang Wang* and Lars Bannenberg*

MXenes, two-dimensional transition metal carbides and nitrides, are promising materials for electrochemical energy storage application due to their redox-active surface and flexible interlayer space. Among all reported MXene-based electrodes, some have shown significantly better high-rate energy storage capabilities. Hence, it is crucial to have a systematic understanding on the decisive factors of the rate capability in the MXene family. This article discusses the impact of material properties at three levels, including intralayer composition, interlayer space and morphology, on the charge transfer and ion transport, revealing all the possible rate-limiting factors of MXene-based electrodes. We also describe systematic methods to characterize MXene electrodes as a detailed fundamental understanding of the structural and chemical properties, and the charge storage mechanisms crucial for rationally designing MXene-based electrodes.

Introduction

The fast development of electrochemical energy storage (EES) devices has revolutionized almost every aspect of modern life by enabling portable electronic devices, electrical vehicles, and grid storage of renewable energy.[1] To satisfy the growing industrial and consumer needs for EES systems with high output power and short recharge time, the electrode materials should have an excellent high-rate performance. Two-dimensional (2D) materials are versatile choices for EES applications, ranging from metal-ion batteries to supercapacitors. A wide variety of ions can be reversibly intercalated and deintercalated in 2D layers, realizing charge storage and release. Due to their open layered structure and weak van der Waals interaction between subsequent layers, 2D materials, including graphene, phosphorene, molybdenum disulfide, and transition metal carbides/nitrides (or MXene), allow high-rate energy storage with low-ion intercalation resistance.

Among 2D materials, MXenes, and especially titanium carbide, are particularly promising EES electrode materials offering a high charge storage capacity with an ultrahigh-rate capability due to their redox-active surface and metallic high electrical conductivity.[2] The general formula of MXenes is $M_{n+1}X_nT_x$, where, M represents one or multiple early transition metal(s) (such as Sc, Ti, Zr, Hf, V, Nb, Ta, Cr, Mo), X is carbon and/or nitrogen, and T_x represents surface functional groups such as O, OH, Cl, and F. If two M-species are present in the MXene, they form either a random metal alloy (solid solution) or an ordered arrangement. MXenes are commonly synthesized from MAX phases, being layered hexagonal carbide or nitride materials with general formula $M_{n+1}AX_n$, where A is an element from the A-group (predominately group 13 and 14). The etching process removes the A layer from the MAX phases while surface groups T_x are simultaneously introduced onto the surface of MXenes.[3] Between each of the layers, there is a flexible interlayer space wherein ions can intercalate (**Figure 1**).

During the charge storage process of 2D MXenes, the intercalated ions can partially transfer their electron to the surface groups of MXenes, changing the valance of the transition metal. This process, called a surface redox, is classified as a pseudocapacitive charge storage process and allows MXenes to store more charge than the electrical double-layer (EDL) mechanism while at the same time offering a much higher rate capability than the typical redox reactions occurring in a battery. As such, a hydrogel $Ti_3C_2T_x$ electrode demonstrated an exceptional volumetric capacitance of up to 1500 F/cm^3 and a macroporous $Ti_3C_2T_x$ electrode delivered ultrahigh rates of 60% at 100 V/s in combination with an acidic aqueous electrolyte.[4] However, despite of the quick expansion of the 2D MXene family, only a limited number of MXenes have

Xuehang Wang, Storage of Electrochemical Energy, Department of Radiation Science and Technology, Delft University of Technology, The Netherlands; x.wang-22@tudelft.nl
Lars Bannenberg, Storage of Electrochemical Energy, Department of Radiation Science and Technology, Delft University of Technology, The Netherlands; l.j.bannenberg@tudelft.nl
*Corresponding authors
doi:10.1557/s43577-021-00150-z

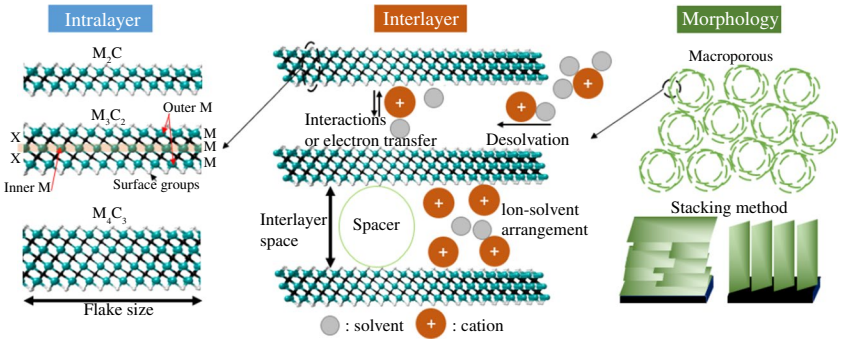

Figure 1. Rate determining factors of 2D materials at three levels: intralayer, interlayer, and electrode morphology.

shown an excellent rate performance. As such, a fundamental understanding of the governing factors of the charge storage process of these 2D materials are essential to offer systematic strategies to improve their high-rate performance, which, in turn, is vital for their successful large-scale implementation.

In this article, we describe how the properties of MXenes at three different levels, including the intralayer and surface chemistry, interlayer space and the morphology, impact the rate capability of MXene-based energy storage devices (Figure 1). First, we discuss how the intralayer chemistry and defects affect the charge and electron transport processes. Second, we summarize how the interlayer space and the ion–solvent arrangement between the 2D layers play a role in the ion intercalation process. Third, we review the effect of the morphology and flake-stacking method of the electrode on the ion transport process. We also offer an overview of the characterization methods used in studying the properties of MXenes that are crucial for understanding the rate capability and energy storage mechanisms of MXene-based electrodes and thereby enable the rational design of MXenes as electrodes.

Intralayer of MXene electrodes

The energy storage process in MXenes can be simplified to three major steps: Ion diffusion from the bulk electrolyte to the 2D interlayer, electron transfer at the MXene surface, and electrons transportation from the active sites to the current collector. The electrical conductivity of the MXene electrode should be maximized for high-rate energy storage as it determines the electron transportation rate. In one layer of M_3C_2 MXenes, the interleaved M and C layers form a transition metal carbide core, which is responsible for the electron transport (**Figure 2**a). The absence of a carbide core in a M_2C MXene may explain the experimentally observed higher electrical conductivity for $Ti_3C_2T_x$ than for Ti_2CT_x.[5] For ordered double transition metal MXenes, the second metal replaces the outer layer of the first metal and forms the structure of $M1_2M2C_2$ and $M1_2M2_2C_3$, where M1 and M2 represent two different early transition metals and could be Mo, Cr, Ta, Nb, V, and Ti. The metallic-like characteristics of MXenes in which Ti is the only metal shifts to semiconductive when the outer layer of MXene becomes Mo as in Mo_2TiC_2 and $Mo_2Ti_2C_3$.[6] Among all reported MXenes, the highest electrical conductivity of ~20,000 S/cm is achieved in $Ti_3C_2T_x$ synthesized by etching Al from the Ti_3AlC_2 MAX phase with excess aluminum.[7] The electrical conductivity of $Ti_3C_2T_x$ MXene can decrease to below 1000 S/cm if the sample contains

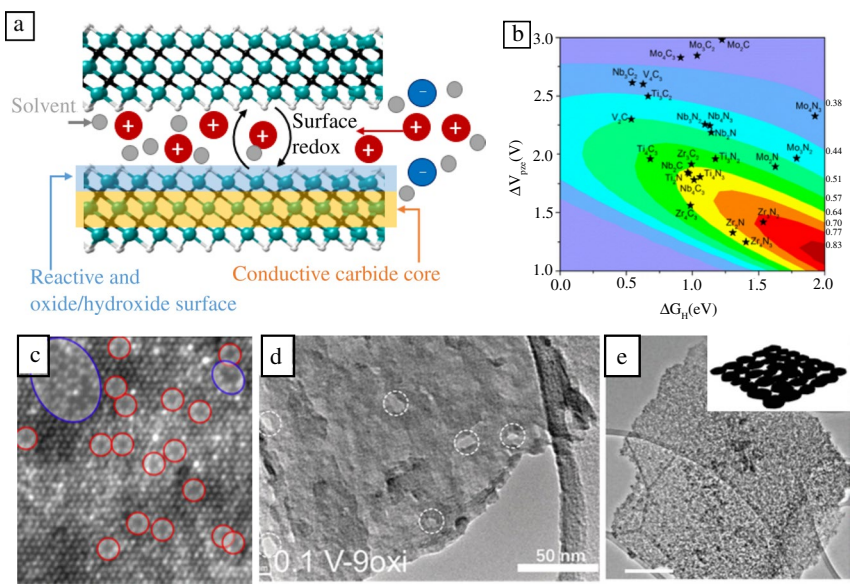

Figure 2. (a) Schematic illustration of the structure of a MXene with three metallic layers and terminated by oxygen surface groups ($M_3C_2O_2$). (b) Charge storage per formula unit versus the shift in the potential at the point of zero charge (ΔV_{PZC}) and hydrogen adsorption free energy (ΔG_H).[17] (c) High-angle annular dark-field imaging scanning transmission electron microscope images from single-layer $Ti_3C_2T_x$ MXene flakes prepared using etchants with 7 wt% HF.[29] (d) Transmission electron microscope (TEM) image of partially oxidized $Ti_3C_2T_x$ MXene at 0.1 V for nine oxidation cycles.[31] (e) TEM image of 2D arrays of transition metal nitride nanocrystals at 700°C.[34]

a high concentration of defects, which is mostly observed when etched by HF.[3] Nevertheless, the electrical conductivity of reported titanium carbide MXene-based EES electrodes are 2–3 order of magnitude higher than activated carbon (typical electrode material of supercapacitors), suggesting that the electron transfer may not limit their high-rate performance. It is also worth mentioning that the high electrical conductivity of $Ti_3C_2T_x$ makes them promising current collectors[8] and conductive binders[9] for EES devices. Hence, we mainly discuss the impact of intralayer properties (i.e., surface groups, defects, and holes) on the charge transfer and ion diffusion processes in this section.

Charge storage process and the impact of surface groups

The surface of MXenes allows for pseudocapacitive ion intercalation with a surface redox reaction, and offers surface area for the formation of EDLs. In the acidic electrolyte, a pair of anodic and cathodic peaks at almost the same potential ($\Delta E_p \approx 0$) can be observed on the CV curve of $Ti_3C_2T_x$ MXene electrodes, indicating pseudocapacitive charge storage.[4,10] Similarly, Li^+ intercalation in $Ti_3C_2T_x$ MXene also leads to obvious peaks in CVs with small ΔE_p in the organic electrolytes, corresponding to pseudocapacitive Li^+ intercalation.[11] Meanwhile, many MXene-based electrodes show rectangular-shaped CVs, especially in neutral aqueous electrolytes. The rectangular-shaped CVs are a signature of EDL formation, but the capacitance of MXenes in neutral aqueous electrolyte is much higher than the value that can be contributed by the EDL formation with a low specific surface area. Several works have reported the specific surface areas of MXenes (e.g., 19.6 m^2/g for vacuum filtered film),[12] 32 m^2/g for self-assembled MXene films, and around 100 m^2/g for various porous-structured MXenes.[13,14] It means that the majority of the specific capacitance of MXenes is contributed by the pseudocapacitive energy storage, even in neutral aqueous electrolytes with almost rectangular-shaped CVs.

Consistent with the fact that the pseudocapacitive energy storage is an important contribution to the overall capacitance of a MXene, the oxidation state of MXenes, or specifically the valence of the transition metal, changes when the electrode is cycled irrespective of whether this occurs in an acidic[15] or neutral aqueous electrolyte.[16] The surface redox reaction occurs as the intercalated ions interact with the surface groups of the MXene and transfer their electron partially to the MXene (Figure 2a). Since there is no phase transformation of MXenes occurring during ion intercalation, the charge storage regime of the MXene electrode is pseudocapacitive. The pseudocapacitive intercalation allows MXenes to store/deliver a much higher capacitance than EDL capacitors. Although $Ti_3C_2T_x$ shows the highest volumetric capacitance among all reported MXenes so far, many other nitride members of the MXene family are predicted to deliver an even higher capacitance than carbides (Figure 2b). DFT simulations further suggest that the charge storage capability of MXenes is highly correlated with the hydrogen adsorption energy and the shift in the potential at the potential of zero charge.[17]

Due to the surface redox charging regime, the surface chemistry of MXenes affects the charge storage capacity of MXene-based electrodes. The functional groups are introduced onto the surface of MXenes after etching the A-group layer (Al, Si or Ga) out of the MAX phase in the enchant solution. For example, –F, –OH, =O and –F, –Cl, –OH, =O are randomly distributed on the MXene surface after HF[18] and LiF-HCl treatment,[19] respectively. For $Ti_3C_2T_x$ electrodes with O, OH and F surface groups, the valence change of Ti is due to the protonation of oxygen functional groups, and the process can be expressed as

$$Ti_3C_2O_x(OH)_yF_z + \delta e^- + \delta H^+ \rightarrow Ti_3C_2O_{x-\delta}(OH)_{y+\delta}F_z,$$

where δ is the number of electron transference with value < 1. Hence, $Ti_3C_2T_x$ etched by an HCl-LiF mixture shows a higher specific capacitance than $Ti_3C_2T_x$ etched in HF due to a higher percentage of O surface functional groups.[18] Fluoride-free etching (e.g., using highly concentrated NaOH at high temperature)[20] and applying the organic tetramethylammonium hydroxide (TMAOH) etchant,[21] prevents the formation of F groups on the MXene surface. Electrochemical etching in the fluoride-free NH_4Cl and TMAOH mixture electrolyte can also remove the Al layer of MAX phases owing to the strong binding of Cl^- with Al, leading to a surface without F surface groups.[22] Post thermal treatment can also increase the ratio of the oxygen surface groups. The F groups can be gradually removed by heating MXenes in Ar/H_2 or N_2/H_2 protective atmospheres.[23,24] The maximum O terminations that a $Ti_3C_2T_x$ MXene can hold without breaking its structural integrity has been estimated to be $x = 3.5$.[25]

Titanium carbide MXenes with the surface covered by Cl or Br functional group have been synthesized by the molten salt method. $Ti_3C_2Cl_2$ was first obtained by etching the Ti_3ZnC_2 in the $ZnCl_2$ Lewis acidic molten salt.[26] Such a method has been generalized to MAX phases with other A elements, including Zn, Al, Si and Ga, to prepare the Cl-terminated MXene.[27] The reactivity of the MAX phases in different molten salts can be predicted by the redox coupling between the cation of the molten salt and the A element. Compared to Ti_3C_2 with O and OH groups, the $Ti_3C_2Cl_2$ shows a distinct electrochemical charge storage process in a Li^+-based organic electrolyte. The CV curve of the $Ti_3C_2Cl_2$ electrode shows obvious Li^+ intercalation over an extensive range of potentials (close to 2 V), whereas the $Ti_3C_2T_x$ shows clear peaks on the CV curves. The almost constant current responding of Li^+ intercalation/deintercalation in the $Ti_3C_2Cl_2$ leads to enhanced capacity. The charge storage process in $Ti_3C_2Cl_2$ is a surface-controlled process, and as such, a high-rate capability can be expected. Using the molten salt method, Br-terminated MXene can also be prepared. The Br termination can be substituted with other groups, including the oxygen, sulfur, selenium, tellurium, and NH groups, as well as with vacancy sites, by exchange reactions.[28]

Intralayer defect and holes

Surface defects and vacancies can provide active sites for ion adsorption and interfacial reactions, which may affect the charge storage capacity, the potential window, and the rate capability. Ti vacancy defects are frequently observed to form clusters within the same sublayers (Figure 2c), and the surface defects concentration can be tuned by changing the percentage of HF during the etching process.[29] Based on molecular dynamics simulations, MXene surfaces with atomic vacancies have stronger attraction to water molecules than MXenes with pristine surfaces. This could be due to the change of the charge distribution around the vacancies. Defective clusters can also change the surface groups of MXenes by forming C–H bonds on the carbon layer of MXenes. These defects can be derived into pinholes on the MXene flakes by further altering the synthesis procedure.

Generating holes through MXene flakes offers new pathways for ion transport, which may shorten the ion diffusion distance and thus improve the high-rate performance. Numerous pinholes were introduced into $Ti_3C_2T_x$ MXenes by adjusting the molar ratio between the MAX phase and the etchant, as well as by prolonging the sonication process.[30] Partial oxidization of MXene flakes can also generate holes of about 20 nm on the MXene flakes (Figure 2d) and as such enlarge the surface area of MXenes.[12] Partially oxidized $Ti_3C_2T_x$ by anodic oxidation shows higher capacitance retention of 66% at 2 V/s than that of 33% for a non-oxidized one.[31] Holes can be introduced on the MXene flakes by further etching with concentrated H_2SO_4. Due to the presence of holes, reduced flake size, and enlarged interlayer space, MXenes prepared by etching with concentrated H_2SO_4 show a high-rate capability even with a high mass loading.[32] Pores and cracks on the length scale of several hundred nanometers can be generated on V_2C MXene using alkali treatment. The corrosive alkali treatment can further etch the MXene flakes and also delaminate the MXene flakes, which allows the intercalation of large K^+ with low resistance.[33] Furthermore, ultraporous 2D transitional metal nitride (TMN) can be prepared by ammonization transition metal oxides (TMOs). Due to the differences in crystal structure and volume of TMOs and TMNs, the TMOs can be transformed into an interconnected TMN with a size of a few nanometers during the reaction with ammonia (Figure 2e). The 2D-like TMN nanocrystals are interconnected, offering a high surface area and a high electrical conductivity.[34]

Interlayer of MXene electrodes

The change of interlayer space and interfacial species in different electrolytes

Various ions, including H^+, Li^+, Na^+, K^+, Mg^{2+}, ionic liquids, and solvents in the bulk electrolyte can intercalate in the interlayer of MXene with low resistance. Because hydrogen-bonding networks of disordered water at inner/outer Helmholtz layers does not induce frictional interactions with the intercalated ion, the energy barrier for interfacial ion transport is small in diluted aqueous electrolyte.[35] The insertion of ions and solvents into MXenes is usually accompanied by the expansion and contraction of the interlayer space. The interlayer of 2D materials is a confined space, and ion transport under different levels of nanoconfinement (or interlayer space) directly affects the ion diffusivities, as ion transport is hindered by interactions from the charged electrode surface and the surrounding interfacial electrolyte.[36]

With a hydrophilic surface, automatic filling of the interlayer space with ions and water molecules starts as soon as the titanium carbide MXene is in contact with the aqueous electrolyte, leading to an increased interlayer space. The response of the interlayer space to the applied potential is complicated and depends on the composition of electrolytes. When $Ti_3C_2T_x$ is negatively charged in the H_2SO_4 electrolyte (**Figure 3**a), the *d*-spacing (derived from the (002) peak in x-ray diffraction; see the "Structural characterization" section first shrinks by 0.1 Å from 0 to −0.6 V versus Ag wire and then rapidly expands by 0.5 Å from −0.6 to −0.9 V. The shrinkage or expansion of the interlayer space in the acidic aqueous electrolyte is attributed to the interactions between the intercalated ions and the dominating surface groups. For example, H^+ intercalation tends to shrink the interlayer space of O-terminated MXenes, while it expands it for OH-terminated MXenes.[37]

Negatively charging MXenes in a commonly used organic electrolyte for batteries (1 M $LiPF_6$ in ethylene carbonate/dimethyl carbonate) also leads to the fluctuating expansion/shrinkage phenomenon. However, the way the *d*-spacing of Ti_2CT_x expands/shrinks during cycling in organic electrolytes is distinct from that in acidic aqueous electrolytes (Figure 3b).[38] Interestingly, the *d*-spacing of $Ti_3C_2Cl_2$ fluctuates with a much smaller amplitude during cycling than that of MXenes with randomly distributed surface groups in the same electrolyte.[27] When ionic liquids are used as electrolyte, the interlayer space change is more straightforward than the aqueous and organic electrolyte due to the absence of solvents.[39] The interlayer space change reflects the different charging storage processes when the electrode is positively and negatively charged from the open circuit potential. The increased interlayer space of the negatively polarized electrode corresponds to the cation insertion, whereas the shrinkage of the interlayer at the positive potential indicates either cation desorption or cation–anion exchange.[40]

The total number of interfacial ions and solvent molecules determine the interlayer space and the arrangement of these species between the interlayer of MXene decide the performance of the electrode. Although the solvent is not directly involved in the charge storage, the type of solvent has a crucial impact on the capacitance and rate capability of MXenes.[11] The *d*-spacing of $Ti_3C_2T_x$ MXenes at the most negative potential is 19.0, 13.0, and 10.7 Å in LiTFSI containing dimethyl sulfoxide (DMSO), acetonitrile (ACN), and propylene carbonate (PC) solvents, respectively. Hence, the arrangement of the interfacial species are also distinct in different solvents (Figure 3c). In DMSO, two layers of solvent molecules are

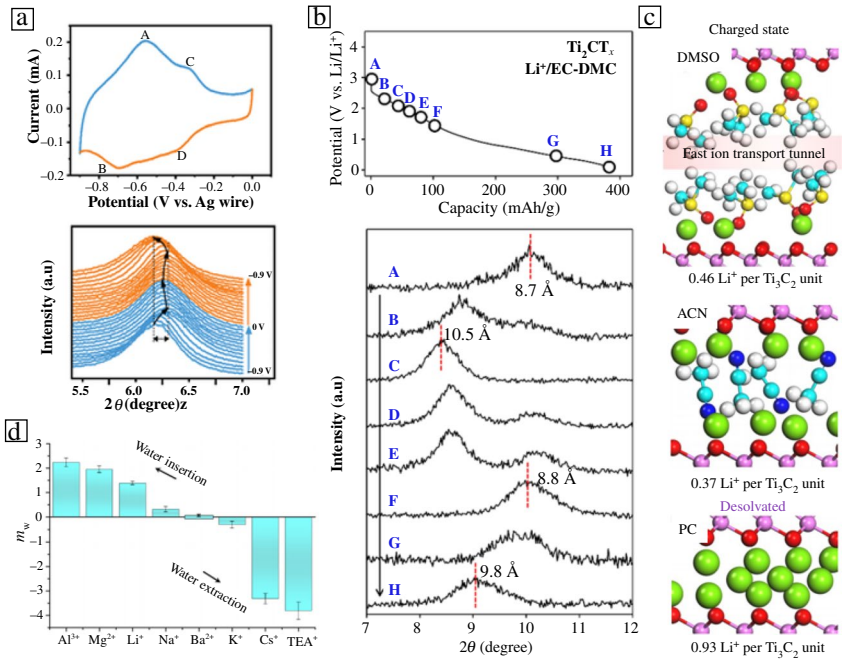

Figure 3. (a) Cyclic voltammogram curve of $Ti_3C_2T_x$ in 1 M H_2SO_4 at 0.2 mV/s and *in situ* x-ray diffraction (XRD) patterns (Cu-Kα, λ = 0.154 nm) acquired during various stages of the electrochemical cycle.[37] (b) First charge curve at 20 mA/g for Ti_2CT_x in 1 M $LiPF_6$ in ethylene carbonate (EC)/dimethyl carbonate (DMC) electrolyte and corresponding *ex situ* XRD patterns.[38] (c) Schematics of the local ion and solvent arrangements as revealed by the molecular dynamics simulation. Legend: green, Li^+; pink, Ti; cyan, C; red, O; teal, F; white, H; yellow, S; blue, N.[11] (d) Number of water molecules cointercalated/extracted per intercalated cation estimated by electrochemical quartz crystal microbalance.[41] DMSO, dimethyl sulfoxide; ACN, acetonitrile; PC, propylene carbonate; TEA, tetraethylammonium.

allowed to be present in such a large interlayer space. Since the oxygen group of DMSO tends to be attracted by Li^+ on the surface of the MXene, the methyl groups of DMSO point away from the MXene surface and form a hydrophobic environment between the two layers of solvent. Such a hydrophobic environment offers a pathway with low-ion transport resistance and hence a good rate capability. In comparison, the smaller interlayer space of MXenes in ACN solvent corresponds to only one layer of solvent molecules between the MXene layers. The ACN molecules block the interfacial ion transport pathways and lead to sluggish ion transport. Despite that the PC solvent has a lower ionic conductivity than ACN, the capacitance of MXenes in PC-based electrolytes is almost twice as high as compared with MXenes used in combination with the other two types of solvents. $Ti_3C_2T_x$ in PC-based electrolytes still offer a high-rate capability. That is because the PC solvent is fully desolvated before Li^+ intercalate, and the bare ion environment allows closer packing of Li^+ and lower ion transport resistance.

The type of ions also has a substantial impact on the desolvation process and hence the interfacial species. In aqueous electrolytes, the insertion of ions with different hydrophilicity can change the interfacial molar ratio between ion and water as determined based on an *in situ* electrochemical quartz crystal microbalance study (Figure 3d).[41] Li^+, Na^+, Mg^{2+}, and Al^{3+} are hydrophilic cations, which can bring in water molecules during ion intercalation. The intercalation of hydrophobic cations such as K^+, Cs^+, and TEA^+ (here TEA represents tetraethylammonium) pushes out interfacial water molecules and increases the ion-to-water ratio. Interestingly, the insertion of Ba^{2+} ions does not influence the interfacial water and is considered as fully desolvated before insertion. The inserted cations also show different affinity toward the surface of MXenes. Based on MD simulations, the intercalated Li^+, Na^+, and K^+ tend to adsorb on the MXene surface, whereas the intercalated Cs^+ and Mg^{2+} are most likely to be located at the center of the interlayer space.[42] The inverse of the simulated average cation-surface oxygen distance is found to have a linear relationship with the experimental capacitance of MXenes at the open circuit potential, which can be explained by a modified Helmholtz model. It is also interesting to note that intercalated Na^+ can penetrate into the intralayer of MXene, which may lead to a fast MXene structural destruction during cycling.

Engineering the interlayer space

Since the interlayer space of MXenes changes with the applied potential, the ion transport resistance is expected to change constantly during cycling. The intercalation of some ions may lead to the shrinkage of the interlayer space, which causes the restacking of the 2D layers and enlarges the ion transport resistance. To assist the ion transport without altering the ions, solvents, and applied potentials used, the interlayer space can be enlarged by preintercalating ions and pillaring low-dimensional materials. Preinsertion of solvents into the MXene interlayers can also facilitate ion transport by offering 2D tunnels for ion transport, which benefits the charge storage process at both room and low temperature.[43]

Preintercalation of MXenes with ions present in the electrolyte or with some large ions can assist the electrolyte ion transport because the larger interlayer space enables better ion accessibility from the bulk electrolyte to the surface active sites. By introducing K^+ into the $Ti_3C_2T_x$ interlayer, the

interlayer space more than doubles from 2 to 4.8 Å.[44] When the species of the preintercalated ions change from the larger K^+ and Na^+ to the smaller Li^+, the capacitance of the MXene in the H_2SO_4 electrolyte decreases, demonstrating that the size of the preintercalated ions plays an important role in the preintercalation-induced performance enhancement. Cationic surfactants, such as cetyltrimethylammonium bromide, can be introduced into the MXene interlayer via liquid phase pillaring to increase the interlayer space dramatically up to 2.7 nm.[45] The ion preintercalation process is necessary for the ionic liquid-based electrolyte as the intercalation of large ions is very resistive. Ionic liquids can be pre-introduced into MXenes and form MXene-ionic liquid ionogels, enhancing both the capacitance and rate capability.[46]

Pillaring the interlayer of 2D MXenes with 0D and 1D materials is an alternative approach to expand the interlayer space of MXenes and avoid restacking. Oxide nanoparticles, which are active materials for electrochemical charge storage, can be introduced to enlarge the interlayer space and contribute to extra capacitance. For example MnO_x nanoparticle can be formed between the MXene interlayers by annealing the $Mn(NO_3)_2$ containing MXene film.[47] Slight oxidation of MXenes is found to increase the interlayer space and forms amorphous carbon, showing enhanced capacitance and rate performance.[32] Further oxidizing MXenes can also increase the capacitance due to the formation of oxide nanoparticles and carbon on the MXene surface.[48,49] However, over oxidation of MXenes may lead to a lower rate capability of MXenes, since the electrical conductivity of TMOs is much lower than that of 2D carbides. Integrating 1D carbon nanotubes (CNT) in the MXene interlayers can significantly enhance the rate capability of MXenes in both aqueous[50] and organic electrolytes.[51] By introducing CNTs, the alignment of the MXene flakes is disrupted, leading to enhanced ion accessibility and open ion transport pathways. The reduced ion transport resistance enables the MXene-CNT composite electrode deliver high capacitance retention in the organic electrolyte at a high scan rate of 10 V/s, as well as at a low temperature of −60°C.[51]

The interlayer space between MXene and other 2D or layered materials

Stacking two different 2D materials into heterostructured architectures offers interlayers with asymmetric interactions from two surfaces. Such 2D heterostructures may construct an electrode that combines the advantage of two individual 2D materials and eliminate the associated shortcomings.[52] One good example is the molybdenum disulfide MoS_2-$Mo_2TiC_2T_x$ heterostructure prepared by *in situ* growth of 2D MoS_2 on the $Mo_2TiC_2T_x$ MXene.[53] Li^+ interacts stronger with the MoS_2-$Mo_2TiC_2T_x$ heterogeneous interface than with homogeneous $Mo_2TiC_2T_x$, leading to an enhanced intercalation process and a higher specific capacity. The poor cycling stability of homogeneous MoS_2 electrodes is also avoided since the $Mo_2TiC_2O_2$ adsorbs Li_2S species stronger with lower binding energies. It is also worth mentioning that heterostructures can be prepared by atomic layer deposition between the ultrathin layer of oxides and MXenes, such as the SnO_2–$Ti_3C_2T_x$[54] and CoO_x–NiO–$Ti_3C_2T_x$[55] heterostructures. The thin-layer oxides-MXene heterostructures show synergetic effect: The oxides mainly contribute to improve the Li^+ storage capacity, while MXene sheets act to buffer the volume changes of oxides and offer high electrical conductivity.

MXenes have also been combined with carbon-/carbide-based 2D materials and these heterostructures show good high-rate performance. The MXene-reduced graphene oxide heterostructure, which is prepared by electrostatic self-assembly of negatively charged $Ti_3C_2T_x$ MXene and positively charged graphene, has an interlayer space that is larger than that of homogenous MXene films. This is because the restacking of the MXene flakes is prevented, which assists rapid ion diffusion between the MXene-graphene interfaces.[56] The graphene layers were also integrated into the MXenes layered structure by alternating electrospray of both 2D materials.[57] The graphene-$Ti_3C_2T_x$ heterostructures have both a higher electrical conductivity and Hall carrier mobility as compared to the homogenous MXene film, which benefits the rate of the charge transfer process. The heterostructure between the 2D graphitic carbon nitride (g-C_3N_4) and $Ti_3C_2T_x$ MXene shows high pseudocapacitance retention at a high rate of 120 C as there is no significant diffusion limitation. The kinetics of the Li^+ diffusion is promoted mainly by the strong interfacial chemical and electronic coupling between g-C_3N_4 and the $Ti_3C_2T_x$ MXene.[58]

Morphology of MXenes

MXene multilayer particles show an accordion-like structure upon etching the bulk solid MAX blocks (**Figure 4**a−b). The capacitance of MXene films prepared via rolling multilayered $Ti_3C_2T_x$ MXene shows a clear dependence on the thickness of the electrode. When the thickness increases from 5 to 75 µm, the capacitance decreases from ~900 to ~370 F/cm^3.[59] However, the rate capability stays almost the same when the thickness of the electrode increases significantly. This is partially attributed to a lower packing density with a more open structure at a larger thickness, indicating the importance of the electrode morphology for the high-rate performance of MXenes.

Assembling 2D materials into 3D architectures improves the ion accessibility and thus enables a fast electrochemical process. Macroporous in MXenes can be introduced using polymer nanospheres as a template and subsequent removal of the nanospheres by annealing (Figure 4c).[60,61] Macroporous $Ti_3C_2T_x$ MXenes show ultrahigh-rate capabilities of 60% at a scan rate up to 100 V/s in the H_2SO_4 electrolyte.[4] The capacitance of macroporous MXene depends less on the thickness of the electrode. When the thickness of the electrode increases from 13 to 180 µm, the capacitance of macroporous $Ti_3C_2T_x$ obtained at 2 mV/s only drops by about 13 percent. Since macropores inevitably lower the packing density of $Ti_3C_2T_x$ MXene from ~3 to ~0.35 g/cm^3, the volumetric capacitance of macroporous MXenes is moderate. The porosity of the 3D architecture should be controlled to avoid bringing in excessive porosity that may

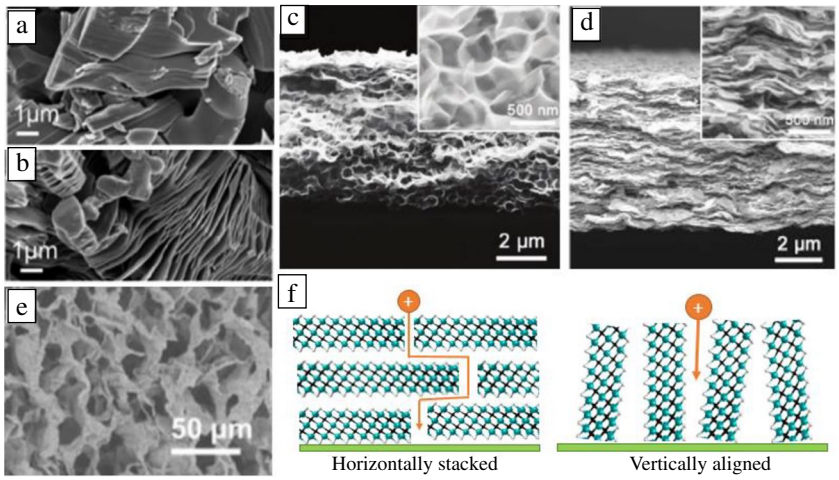

Figure 4. (a, b) Scanning electron microscope (SEM) image of Ti_3AlC_2 MAX phases and multilayered $Ti_3C_2T_x$ powder synthesized by etching in 30 wt% HF.[3] (c) Cross-sectional SEM image of a macroporous $Ti_3C_2T_x$ MXene electrode.[61] (d) SEM images of a wavy $Ti_3C_2T_x$ film.[63] (e) SEM image of freeze-dried MXene hydrogel.[64] (f) Ion transport in horizontally stacked and vertically aligned $Ti_3C_2T_x$ MXene films. The orange lines indicate ion transport pathways.

reduce the volumetric energy density.[62] By pressing macroporous $Ti_3C_2T_x$, the MXene shows a wavy structure (Figure 4d), which still offers a good ion accessibility and high-rate capability in both aqueous[63] and organic electrolytes.[11] However, the packing density of the pressed macroporous $Ti_3C_2T_x$ becomes much higher (>2 g/cm^3), increasing its volumetric capacitance. Three-dimensional MXene hydrogels have been prepared by gelating MXenes in a solution of graphene oxide in ethylenediamine (Figure 4e).[64] The packing density of 3D MXene hydrogels can be increased from 0.027 to 2.1 g/cm^3 by controlling the pore size with different drying processes.

Compared to horizontally stacked 2D MXenes, vertically aligned structures have a shortened ion transport length (Figure 4f). The direction of the electric field is the same with respect to the ion transport in the vertically aligned MXene, which may facilitate the ion acceleration. Vertically aligned MXenes were first prepared by mechanical shearing of a discotic lamellar liquid-crystal phase of $Ti_3C_2T_x$ MXene.[65] The capacitance of the vertically aligned $Ti_3C_2T_x$ is thickness-independent: the capacitance is almost the same when the thickness of the electrode increases from 40 to 320 μm at 10 mV/s. The rate capability of a thick electrode (320 μm) is also almost the same as a thin one (40 μm) for scan rates up to 100 V/s. When preparing liquid-crystal MXenes, a surfactant is added to increase the packing symmetry of MXene flakes. To restore the electrical conductivity and ionic accessibility of MXenes, the surfactant must be removed, which complicates the preparation process. By tuning the aspect ratio of MXene flakes and the concentration of the MXene colloidal solution, $Ti_3C_2T_x$ MXene can form a nematic liquid-crystal phase without adding any surfactants or binders.[66]

Characterization of MXenes-based electrodes

Structural characterization

The structure of MXenes and other 2D materials is of vital importance for understanding their performance in EES, yet, their characterization is in general quite challenging as compared to 3D materials. X-ray diffraction (XRD) is a widely applied method to obtain the interlayer spacing and to check the purity of the synthesized MXenes. Typical experiments are performed on laboratory diffractometers in the Bragg–Brentano configuration, in which the sample is stationary and the x-ray beam and detector synchronously move around it, implying that only information in the direction perpendicular to the surface of the sample can be obtained. Following Bragg's Law, the position of the peaks in the diffraction pattern provide information about the interlayer spacing/*d*-spacing. As the *d*-spacing is the distance between the center of one layer to the center of the next one, the interlayer distance can be obtained from the *d*-spacing by subtracting the thickness of the MXene layer. Differently, the width of the peaks are related to the size and homogeneity of the domains of MXenes: At a constant experimental resolution, narrower peak widths indicate a larger size of the domains and/or an improved homogeneity. As XRD patterns of pure and stacked MXene films only display (00l) reflections, and those of MAX phases have many more reflections (**Figure 5**a), XRD allows one to examine the quality of the synthesized material. We note that in-plane XRD measurements of stacked MXene films (Figure 5c) as well as powered or stacks of randomly oriented MXene flakes may display more diffraction peaks, including the (110) peak that is expected for the MXene's hexagonal in-plane symmetry.[67] In addition, XRD is often performed *in situ*/*operando* (e.g., allowing to study the change in interlayer spacing when ions (de)intercalate when different voltages are applied to MXene electrodes).

Different from common (powder) crystalline materials, Bragg–Brentano XRD cannot be used to fully resolve the structure of MXenes. Indeed, the monocrystalline nature of the MXene sheet, stacking disorder of the sheets, and the short-range ordering of the surface structure complicates the analysis.[68] The $P6_3/mmc$ hexagonal symmetry of MXenes is usually confirmed by transmission electron microscopy (TEM), which uses electrons to image specimens typically thinner than 100 nm in transmissions (Figure 5e). TEM can

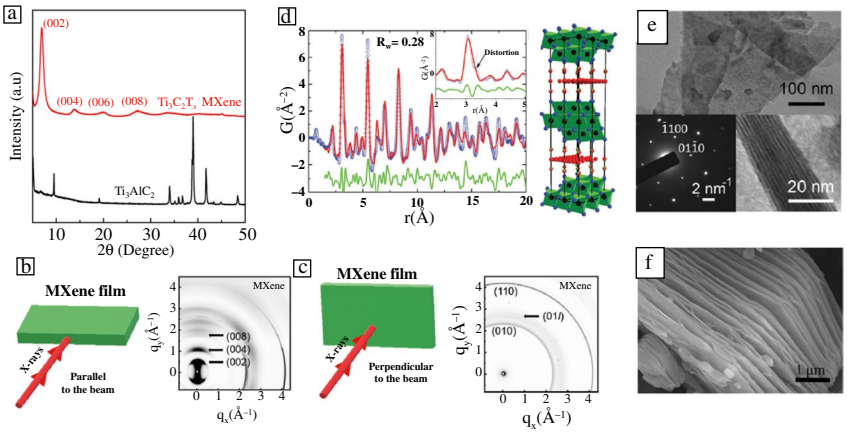

Figure 5. Structural characterization of MXenes. (a) Bragg–Brentano x-ray diffraction patterns (λ = 0.154 nm) of $Ti_3C_2T_x$ MXene and Ti_3AlC_2 MAX phase. Following Bragg's Law, the interplanar distance c = 2.55 nm can be computed from the position of the (002) peak at $2\theta_{200} = 6.94°$: $c = \lambda/\sin(\theta_{200})$.[78] (b, c) Wide-angle x-ray scattering results of $Ti_3C_2T_x$ performed in two configurations: with the MXene films oriented (b) parallel and (c) perpendicular to the x-ray beam. (b) The diffraction pattern shows peaks along the vertical direction, indicating preferred alignment of the sheets, while the (010) and (110) diffraction rings in (c) are characteristic of the hexagonal in-plane symmetry.[75] (d) Pair distribution function of $Nb_4C_3T_x$ obtained from a synchrotron x-ray total scattering experiment. The blue circles indicate the measured data, and the red line the best-fit model. The green curve indicates the difference between the fit and the data. The inset shows a shoulder peak at 0.33 nm, indicating a distortion in the Nb_4C_3 slab. The structure is a polyhedral representation of undistorted $Nb_4C_3T_x$. Nb, C, O/F atoms are in blue, black, red/green colors, respectively. The intercalated water molecules are represented by sheets of oxygen atoms.[69] (e) Transmission electron microscope (TEM) micrograph of a $Nb_4C_3T_x$ flake. The left inset shows the selected area electron diffraction pattern characteristic of the hexagonal symmetry. The right inset shows a cross-sectional TEM micrograph.[70] (f) Scanning electron microscope image of a $Ti_3C_2T_x$ MXene.[79]

be operated in several modes. One widely applied mode is scanning transmission electron microscopy (STEM), in which the sample is scanned with a beam with a spot size typically smaller than 0.2 nm while performing spectroscopic mapping using energy-dispersive x-ray (EDX) or electron energy-loss spectroscopy (EELS) in parallel to obtain elemental information. Differently, TEM can be used for (selected-area) electron diffraction ([SA]ED) to obtain information about the crystal structure. Here, electrons are diffracted and reciprocal images similar to 2D XRD patterns are acquired, thus providing information about the (in-plane) crystal structure.

Quantitative information about the (in-plane) structure can be obtained by total diffraction measurements in combination with atomic pair distribution function (pdf) analysis. In these experiments, powdered MXene is typically sealed in a capillary and measured with high-energy synchrotron x-rays or neutrons in transmission. Subsequently, the Fourier transform of the diffraction pattern is taken, providing $G(r)$ (Figure 5d). $G(r)$ is the atomic pair distribution function and represents the probability to find a pair of atoms separated by a distance r. By modeling $G(r)$, important information about the structure of the atoms and some surface species within the layer can be obtained.[6,69,70] As x-rays are predominately sensitive to the electrons surrounding a nucleus of an atom, they are mostly insensitive to light atoms. Neutron diffraction provides complimentary information on especially the surface groups as neutrons mainly interact with the atomic nucleus, and are particularly sensitive to (light) elements such as H, Li, and Na.[68,71,72] For example, it has been shown by neutron total diffraction that multiple sodiation sites exist in $Ti_3C_2T_x$ in conjunction with a 2D sodium domain structure at the interfaces/surfaces of $Ti_3C_2T_x$.[71]

At larger length scales, information about the structure and morphology can be obtained by microscopy techniques such as atomic force microscopy (AFM) and scanning electron microscopy (SEM). Owing to its lower resolution as compared to AFM and TEM, SEM is mostly used to study the morphology and stacking of MXene layers into 3D structures (Figure 5f). A more quantitative method to study the stacking and organization of the 2D MXene layers is using wide-angle x-ray scattering (WAXS) and small-angle x-ray and neutron scattering (SAXS/SANS).[73–76] In a WAXS experiment, a sample is measured by x-rays in transmission and a 2D dimensional diffraction pattern is obtained. If the sample is fully textured and the x-ray beam is parallel to the MXene film, two spots will show up on the diffraction pattern (Figure 5b), whereas in the limit of no texture homogeneous rings will appear on the detector. This texture can, for example, be quantified by the Herman's orientation factor.[77] SAXS uses the same scattering geometry as WAXS, but only considers small scattering angles (typically < 1°), allowing one to probe larger length scales.

Surface chemistry and chemical identification

In x-ray photoelectron spectroscopy (XPS), a sample is illuminated by monochromatic x-rays that are partly absorbed by the sample owing to the photoelectric effect, causing the emission of a (photo)electron. By taking the difference between the measured kinetic energy of the emitted electron and the energy of the x-ray, the binding energy of the electron can be computed. This allows the identification of the elements present in the sample (with the exception of H and He), and, since the binding energy of the electrons are affected by the chemical state/environment of the atoms, these can be identified. XPS

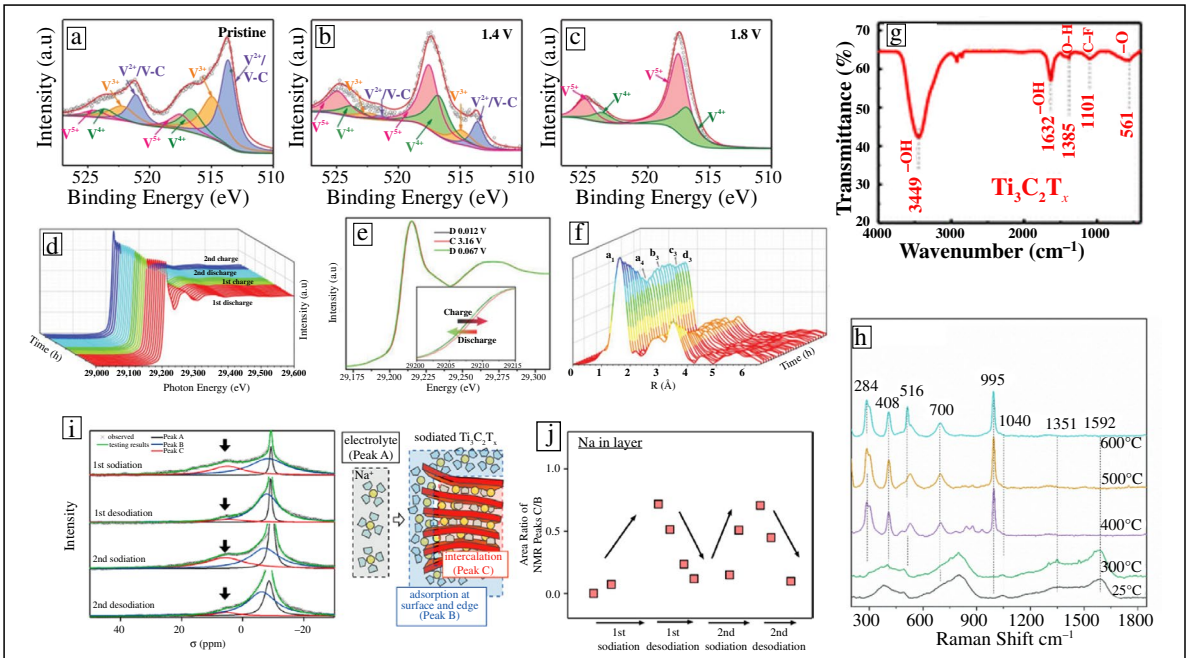

Figure 6. Characterization of MXenes using spectroscopy. (a–c) X-ray photoelectron spectroscopy spectra around V2p of (a) pristine and (c) electrochemically activated V_2CT_x cathodes charged to a voltage of (b) 1.4 and (c) 1.8 V.[80] (d–f) X-ray absorption spectroscopy (XAS) measurements on Sn-intercalated V_2C MXene as Li-ion electrode. (d) *In operando* Sn K-edge XAS spectra. (e) Fourier transformed Sn K-edge extended x-ray absorption fine structure spectra used to determine the coordination number. (f) Normalized x-ray absorption near-edge structure spectra of the Sn K-edge at different voltages with the inset showing an enlargement of the absorption edge.[83] (g) Fourier transform infrared spectrum of delaminated $Ti_3C_2T_x$ demonstrating the presence of typical functional groups on the surface: the bending vibration of –O surface groups at 561 cm^{-1}, and at 1101 cm^{-1} and 1385 cm^{-1} the stretching vibrations of C–F and O–H, respectively. At 1632 and 3449 nm^{-1} the bending and stretching modes of water molecules are observed, respectively.[84] (h) *In situ* Raman spectra (403 nm) of V_2CT_x after exposure to air at the indicated temperature. For T > 300°C, V_2CT_x oxidizes into bulk V_2O_5 as evidenced by the characteristic V_2O_5 peaks at 294, 480, 520, and 696 cm^{-1}.[86] (i, j) ^{23}Na magic angle spinning (NMR) spectra to identify the insertion mechanism of Na into $Ti_3C_2T_x$. (i) Nuclear magnetic resonance spectra during the initial two cycles deconvoluted into three peaks. The peaks originate from different Na^+ species as indicated in the schematic. (j) Estimated amount of intercalated Na in the layer based on the area ratio of the NMR peaks.[91]

is a surface technique and only sensitive to approximately the first 10 nm of the sample. XPS has been used to study the oxidation of V_2CT_x cathodes for high capacity and high-rate aqueous zinc-ion batteries,[80] revealing that the capacity can be enhanced significantly by electrochemical activation. These measurements show that low-valance V (V-C/V^{2+}/V^{3+}) is predominately present in pristine V_2CT_x cathodes, being a bottleneck in realizing a high capacity (**Figure 6**a).[80,81] After an initial activation at 1.8 V, the valence on the surface is raised significantly to V^{4+}/V^{5+}, and a nanoscale vanadium oxide (VO_x) coating is formed that effectively undergoes multi-electron reactions (Figure 6b–c). Subsequently, the analysis performed after edging approximately the first 200 nm of the sample shows that the presence of low-valance V after activation is similar to that of pristine V_2CT_x, indicating that the internal structure is preserved guaranteeing high electrical and ionic conductivities.[80]

One major limitation of XPS is that experiments have to be performed in vacuum that generally hinders *in situ*/*operando* experiments. X-ray absorption spectroscopy (XAS) is an alternative for such experiments but requires an intense and tuneable (high) energy x-ray beam and it is therefore typically performed at synchrotron radiation facilities.[82] XAS considers the x-ray absorbance measured as a function of the x-ray's energy. When the energy of the x-rays equals the binding energy, a sharp increase ("absorption edge") is seen in the x-ray absorption (Figure 6d). By analyzing the detailed shape of the absorption spectrum around the edge (x-ray absorption near-edge structure, XANES) or after the edge (extended x-ray absorption fine structure, EXAFS) information about the chemical state or the molecular structure can be obtained.[81] As an example, XAS has been used to ex situ and *in operando* study Sn-intercalated V_2C MXene electrodes to investigate the evolution of the structure and electrochemical activity of vanadium and tin atoms during (dis)charging in Li^+-based electrolyte.[83] The shift of the absorption edge shows that a reversible valance change of Sn from +3.35 to +3.42 with a voltage increase from 0.012 to 3.16 V versus Li/Li^+ occurs (Figure 6e), constituting a significant contribution to the Li-ion capacity and stability. In addition, the Fourier transform

of the absorption spectra show that the coordination number of Sn decreases because of the Li-ion intercalation (Figure 6f).

Fourier transform infrared spectroscopy (FTIR) is another absorption spectroscopy technique. In FTIR, a sample is illuminated by infrared light and the transmittance, being the fraction of transmitted light, is determined as a function of the wavelength of the light. The transmittance is usually plotted as a function of the wavenumber of the light, being the inverse wavelength with unit cm^{-1}. Typically, sharp minima in the transmittance are seen, caused by the absorbance of the light by vibrational modes in the sample, allowing one to identify the molecules and chemical bonds present in a sample (Figure 6g). As such, FTIR can be for instance used to detect the presence of surface groups or to assess the quality and purity of the synthesized compounds.[84]

Similar to FTIR, Raman spectroscopy uses the interaction of photons (typically laser light) with molecular vibrations, phonons, or other excitations in the system. These interactions may slightly in or decrease the photon's energy, named Raman scattering. The energy shift provides information about the vibrational modes in a sample, in turn allowing to identify the molecule and study the chemical bonding and intramolecular bonds. In Raman spectroscopy, the measured intensity is usually displayed as a function of the "Raman shift", calculated by taking the difference of the inverse wavelengths ("wavenumbers") of the incident and detected photons. The potential of Raman spectroscopy has been demonstrated on $Ti_3C_2T_x$ proving information about the surface chemistry, stacking, and quality (Figure 6h).[85] Although the Raman spectra of MXenes are in general complex and consist of many convoluted peaks (see also Reference 84), *in situ* Raman spectroscopy can be used to assess the thermal and chemical stability of MXenes: For example, it has been shown that V_2CT_x MXenes slightly oxidize or transform in V_2O_5 above 300°C in the presence of air or CO_2.[86]

Nuclear magnetic resonance (NMR) spectroscopy is another technique that can be used to quantitatively identify chemical species.[87–90] Different from XPS, NMR is a bulk technique, can be used to study dynamics and diffusion, and allows for *in situ*/*operando* measurements. In NMR experiments, a sample is positioned in a strong and constant magnetic field and perturbed by a weak oscillating magnetic field. A nucleus with a non-zero spin (e.g., ^{1}H, ^{7}Li, ^{13}C, ^{19}F, ^{23}Na, ^{27}Al) responds to this oscillatory magnetic field by producing an electromagnetic signal with a characteristic frequency. This resonant frequency depends on the molecular structure and electronic environment of the nucleus and is usually expressed as the chemical shift, being the resonant frequency of the nucleus relative to that of a standard sample. As the differences in resonant frequency are quite small, the chemical shift is usually expressed in parts per million (ppm). Example usage in the field of MXenes are the identification and quantification of surface groups in $Ti_3C_2T_x$[18] and V_2CT_x.[90] In addition, NMR has been used to study the Na insertion mechanism into $Ti_3C_2T_x$ (Figure 6i–j). Depending on whether ^{23}Na is present in the electrolyte, adsorbed at the surface of the MXene or intercalated between the layers, different peaks emerge in the NMR spectra.[91] The results show that reversible Na^+ (de)intercalation between the $Ti_3C_2T_x$ layers occurs upon (de)sodiation as well as that a certain amount of ^{23}Na remains intercalated after the $Ti_3C_2T_x$ layers desodiation at 3.0 V.

Summary

In this article, we review rate-limiting factors of MXene-based electrodes by showing how the material properties at three levels, being the (1) intralayer composition, (2) interlayer space, and (3) morphology, impact the charge transfer and ion transport in MXenes: (1) We discuss the impact of intralayer composition on the electrical conductivity of MXenes and summarize the role of surface termination of MXenes in the charge transfer process. We also show that the generation of holes on the MXene flakes benefits the rate capability of MXene as the ion transport distance is shortened. (2) The interlayer space of MXenes is influenced by the intralayer composition of MXene, type of electrolyte ion, choice of solvent, and the applied potential. Preinsertion of spacers into the 2D MXene interlayers can enlarge the interlayer space and reduce the ion intercalation resistance. We also discuss that MXene-layered material heterostructures can benefit from the high-rate capability of MXenes and the high capacity of the other layered materials. (3) Assembling 2D materials into 3D architectures increases the rate capability of MXene-based electrodes since it mitigates the restacking of the 2D layers and improves the ion accessibility. In addition, we discuss the experimental techniques at hand to acquire the detailed fundamental understanding of the structural and chemical properties as well as the charge storage mechanisms of MXenes. As illustrated, these techniques, combined with electrochemical characterization, provide the detailed understanding of MXenes required to enable the rational design of high-rate MXene-based energy storage systems.

Conflicts of interest

On behalf of all authors, the corresponding author states that there is no conflict of interest.

Open Access

References

1. E. Pomerantseva, F. Bonaccorso, X. Feng, Y. Cui, Y. Gogotsi, *Science* **366**, eaan8285 (2019)
2. B. Anasori, M.R. Lukatskaya, Y. Gogotsi, *Nat. Rev. Mater.* **2**, 16098 (2017)
3. M. Alhabeb, K. Maleski, B. Anasori, P. Lelyukh, L. Clark, S. Sin, Y. Gogotsi, *Chem. Mater.* **29**, 7633 (2017)
4. M.R. Lukatskaya, S. Kota, Z. Lin, M.-Q. Zhao, N. Shpigel, M.D. Levi, J. Halim, P.-L. Taberna, M.W. Barsoum, P. Simon, *Nat. Energy* **2**, 17105 (2017)
5. Y. Yang, K. Hantanasirisakul, N.C. Frey, B. Anasori, R.J. Green, P.C. Rogge, I. Waluyo, A. Hunt, P. Shafer, E. Arenholz, *2D Mater.* **7**, 025015 (2020)
6. B. Anasori, C. Shi, E.J. Moon, Y. Xie, C.A. Voigt, P.R. Kent, S.J. May, S.J. Billinge, M.W. Barsoum, Y. Gogotsi, *Nanoscale Horiz.* **1**, 227 (2016)
7. T.S. Mathis, K. Maleski, A. Goad, A. Sarycheva, M. Anayee, A.C. Foucher, K. Hantanasirisakul, C.E. Shuck, E.A. Stach, Y. Gogotsi, *ACS Nano* (2020). https://doi.org/10.1021/acsnano.0c08357
8. C.-H. Wang, N. Kurra, M. Alhabeb, J.-K. Chang, H.N. Alshareef, Y. Gogotsi, *ACS Omega* **3**, 12489 (2018)
9. N. Sun, Q. Zhu, B. Anasori, P. Zhang, H. Liu, Y. Gogotsi, B. Xu, *Adv. Funct. Mater.* **29**, 1906282 (2019)
10. T.S. Mathis, N. Kurra, X. Wang, D. Pinto, P. Simon, Y. Gogotsi, *Adv. Energy Mater.* **9**, 1902007 (2019)
11. X. Wang, T.S. Mathis, K. Li, Z. Lin, L. Vlcek, T. Torita, N.C. Osti, C. Hatter, P. Urbankowski, A. Sarycheva, *Nat. Energy* **4**, 241 (2019)
12. C.E. Ren, M.Q. Zhao, T. Makaryan, J. Halim, M. Boota, S. Kota, B. Anasori, M.W. Barsoum, Y. Gogotsi, *ChemElectroChem* **3**, 689 (2016)
13. S. Shah, T. Habib, H. Gao, P. Gao, W. Sun, M. Green, M. Radovic, *Chem. Commun.* **53**, 400 (2017)
14. Y. Wang, H. Dou, J. Wang, B. Ding, Y. Xu, Z. Chang, X. Hao, *J. Power Sources* **327**, 221 (2016)
15. M.R. Lukatskaya, S.M. Bak, X. Yu, X.Q. Yang, M.W. Barsoum, Y. Gogotsi, *Adv. Energy Mater.* **5**, 1500589 (2015)
16. A. Sugahara, Y. Ando, S. Kajiyama, K. Yazawa, K. Gotoh, M. Otani, M. Okubo, A. Yamada, *Nat. Commun.* **10**, 850 (2019)
17. C. Zhan, W. Sun, P.R. Kent, M. Naguib, Y. Gogotsi, D.-E. Jiang, *J. Phys. Chem. C* **123**, 315 (2018)
18. M.A. Hope, A.C. Forse, K.J. Griffith, M.R. Lukatskaya, M. Ghidiu, Y. Gogotsi, C.P. Grey, *Phys. Chem. Chem. Phys.* **18**, 5099 (2016)
19. S. Kajiyama, L. Szabova, H. Iinuma, A. Sugahara, K. Gotoh, K. Sodeyama, Y. Tateyama, M. Okubo, A. Yamada, *Adv. Energy Mater.* **7**, 1601873 (2017)
20. T. Li, L. Yao, Q. Liu, J. Gu, R. Luo, J. Li, X. Yan, W. Wang, P. Liu, B. Chen, *Angew. Chem. Int. Ed.* **57**, 6115 (2018))
21. J. Xuan, Z. Wang, Y. Chen, D. Liang, L. Cheng, X. Yang, Z. Liu, R. Ma, T. Sasaki, F. Geng, *Angew. Chem. Int. Ed.* **128**, 14789 (2016)
22. S. Yang, P. Zhang, F. Wang, A.G. Ricciardulli, M.R. Lohe, P.W. Blom, X. Feng, *Angew. Chem. Int. Ed.* **57**, 15491 (2018)
23. S. Lai, J. Jeon, S.K. Jang, J. Xu, Y.J. Choi, J.-H. Park, E. Hwang, S. Lee, *Nanoscale* **7**, 19390 (2015)
24. R.B. Rakhi, B. Ahmed, M.N. Hedhili, D.H. Anjum, H.N. Alshareef, *Chem. Mater.* **27**, 5314 (2015)
25. I. Persson, J. Halim, T.W. Hansen, J.B. Wagner, V. Darakchieva, J. Palisaitis, J. Rosen, P.O. Persson, *Adv. Funct. Mater.* **30**, 1909005 (2020)
26. M. Li, J. Lu, K. Luo, Y. Li, K. Chang, K. Chen, J. Zhou, J. Rosen, L. Hultman, P. Eklund, *J. Am. Chem. Soc.* **141**, 4730 (2019)
27. Y. Li, H. Shao, Z. Lin, J. Lu, L. Liu, B. Duployer, P.O. Persson, P. Eklund, L. Hultman, M. Li, *Nat. Mater.* **19**, 894 (2020)
28. V. Kamysbayev, A.S. Filatov, H. Hu, X. Rui, F. Lagunas, D. Wang, R.F. Klie, D.V. Talapin, *Science* **369**, 979 (2020)
29. X. Sang, Y. Xie, M.-W. Lin, M. Alhabeb, K.L. Van Aken, Y. Gogotsi, P.R. Kent, K. Xiao, R.R. Unocic, *ACS Nano* **10**, 9193 (2016)
30. A. Lipatov, M. Alhabeb, M.R. Lukatskaya, A. Boson, Y. Gogotsi, A. Sinitskii, *Adv. Electron. Mater.* **2**, 1600255 (2016)
31. J. Tang, T.S. Mathis, N. Kurra, A. Sarycheva, X. Xiao, M.N. Hedhili, Q. Jiang, H.N. Alshareef, B. Xu, F. Pan, *Angew. Chem. Int. Ed.* **58**, 17849 (2019)
32. J. Tang, T. Mathis, X. Zhong, X. Xiao, H. Wang, M. Anayee, F. Pan, B. Xu, Y. Gogotsi, *Adv. Energy Mater.* **11**, 2003025 (2021)
33. F. Ming, H. Liang, W. Zhang, J. Ming, Y. Lei, A.-H. Emwas, H.N. Alshareef, *Nano Energy* **62**, 853 (2019)
34. X. Xiao, H. Wang, W. Bao, P. Urbankowski, L. Yang, Y. Yang, K. Maleski, L. Cui, S.J. Billinge, G. Wang, *Adv. Mater.* **31**, 1902393 (2019)
35. K. Kim, M. Okubo, A. Yamada, *J. Electrochem. Soc.* **166**, A3739 (2019)
36. X. Wang, M. Salari, D.-E. Jiang, J.C. Varela, B. Anasori, D.J. Wesolowski, S. Dai, M.W. Grinstaff, Y. Gogotsi, *Nat. Rev. Mater.* **5**, 787 (2020)
37. X. Mu, D. Wang, F. Du, G. Chen, C. Wang, Y. Wei, Y. Gogotsi, Y. Gao, Y. Dall'Agnese, *Adv. Funct. Mater.* **29**, 1902953 (2019)
38. M. Okubo, A. Sugahara, S. Kajiyama, A. Yamada, *Acc. Chem. Res.* **51**, 591 (2018)
39. Y. Dall'Agnese, P. Rozier, P.-L. Taberna, Y. Gogotsi, P. Simon, *J. Power Sources* **306**, 510 (2016)
40. Z. Lin, P. Rozier, B. Duployer, P.-L. Taberna, B. Anasori, Y. Gogotsi, P. Simon, *Electrochem. Commun.* **72**, 50 (2016)
41. N. Shpigel, M.D. Levi, S. Sigalov, T.S. Mathis, Y. Gogotsi, D. Aurbach, *J. Am. Chem. Soc.* **140**, 8910 (2018)
42. Q. Gao, W. Sun, P. Ilani-Kashkouli, A. Tselev, P.R. Kent, N. Kabengi, M. Naguib, M. Alhabeb, W.-Y. Tsai, A.P. Baddorf, *Energy Environ. Sci.* **13**, 2549 (2020)
43. J. Xu, X. Hu, X. Wang, X. Wang, Y. Ju, S. Ge, X. Lu, J. Ding, N. Yuan, Y. Gogotsi, *Energy Storage Mater.* **33**, 382 (2020)
44. J. Li, X. Yuan, C. Lin, Y. Yang, L. Xu, X. Du, J. Xie, J. Lin, J. Sun, *Adv. Energy Mater.* **7**, 1602725 (2017)
45. J. Luo, W. Zhang, H. Yuan, C. Jin, L. Zhang, H. Huang, C. Liang, Y. Xia, J. Zhang, Y. Gan, *ACS Nano* **11**, 2459 (2017)
46. Z. Lin, D. Barbara, P.-L. Taberna, K.L. Van Aken, B. Anasori, Y. Gogotsi, P. Simon, *J. Power Sources* **326**, 575 (2016)
47. Y. Tian, C. Yang, W. Que, X. Liu, X. Yin, L.B. Kong, *J. Power Sources* **359**, 332 (2017)
48. M. Naguib, O. Mashtalir, M.R. Lukatskaya, B. Dyatkin, C. Zhang, V. Presser, Y. Gogotsi, M.W. Barsoum, *Chem. Commun.* **50**, 7420 (2014)
49. C. Zhang, S.J. Kim, M. Ghidiu, M.Q. Zhao, M.W. Barsoum, V. Nicolosi, Y. Gogotsi, *Adv. Funct. Mater.* **26**, 4143 (2016)
50. M.Q. Zhao, C.E. Ren, Z. Ling, M.R. Lukatskaya, C. Zhang, K.L. Van Aken, M.W. Barsoum, Y. Gogotsi, *Adv. Mater.* **27**, 339 (2015)
51. X. Gao, X. Du, T.S. Mathis, M. Zhang, X. Wang, J. Shui, Y. Gogotsi, M. Xu, *Nat. Commun.* **11**, 6160 (2020)
52. E. Pomerantseva, Y. Gogotsi, *Nat. Energy* **2**, 17089 (2017)
53. C. Chen, X. Xie, B. Anasori, A. Sarycheva, T. Makaryan, M. Zhao, P. Urbankowski, L. Miao, J. Jiang, Y. Gogotsi, *Angew. Chem. Int. Ed.* **57**, 1846 (2018)
54. B. Ahmed, D.H. Anjum, Y. Gogotsi, H.N. Alshareef, *Nano Energy* **34**, 249 (2017)
55. X. Zhang, B. Shao, A. Guo, Z. Gao, Y. Qin, C. Zhang, F. Cui, X. Yang, *J. Alloys Compd.* **862**, 158546 (2021)
56. J. Yan, C.E. Ren, K. Maleski, C.B. Hatter, B. Anasori, P. Urbankowski, A. Sarycheva, Y. Gogotsi, *Adv. Funct. Mater.* **27**, 1701264 (2017)
57. B. Aïssa, A. Ali, K. Mahmoud, T. Haddad, M. Nedil, *Appl. Phys. Lett.* **109**, 043109 (2016)
58. Y.-P. Zhu, Y. Lei, F. Ming, E. Abou-Hamad, A.-H. Emwas, M.N. Hedhili, H.N. Alshareef, *Nano Energy* **65**, 104030 (2019)
59. M. Ghidiu, M.R. Lukatskaya, M.-Q. Zhao, Y. Gogotsi, M.W. Barsoum, *Nature* **516**, 78 (2014)
60. M.Q. Zhao, X. Xie, C.E. Ren, T. Makaryan, B. Anasori, G. Wang, Y. Gogotsi, *Adv. Mater.* **29**, 1702410 (2017)
61. K. Li, X. Wang, S. Li, P. Urbankowski, J. Li, Y. Xu, Y. Gogotsi, *Small* **16**, 1906851 (2020)
62. M.R. Lukatskaya, B. Dunn, Y. Gogotsi, *Nat. Commun.* **7**, 12647 (2016)
63. K. Li, X. Wang, X. Wang, M. Liang, V. Nicolosi, Y. Xu, Y. Gogotsi, *Nano Energy* **75**, 104971 (2020)
64. T. Shang, Z. Lin, C. Qi, X. Liu, P. Li, Y. Tao, Z. Wu, D. Li, P. Simon, Q.H. Yang, *Adv. Funct. Mater.* **29**, 1903960 (2019)
65. Y. Xia, T.S. Mathis, M.-Q. Zhao, B. Anasori, A. Dang, Z. Zhou, H. Cho, Y. Gogotsi, S. Yang, *Nature* **557**, 409 (2018)
66. J. Zhang, S. Uzun, S. Seyedin, P.A. Lynch, B. Akuzum, Z. Wang, S. Qin, M. Alhabeb, C.E. Shuck, W. Lei, *ACS Cent. Sci.* **6**, 254 (2020)
67. M. Ghidiu, M.W. Barsoum, *J. Am. Ceram. Soc.* **100**, 5395 (2017)
68. H.-W. Wang, M. Naguib, K. Page, D.J. Wesolowski, Y. Gogotsi, *Chem. Mater.* **28**, 349 (2016)
69. C. Shi, M. Beidaghi, M. Naguib, O. Mashtalir, Y. Gogotsi, S.J. Billinge, *Phys. Rev. Lett.* **112**, 125501 (2014)
70. M. Ghidiu, M. Naguib, C. Shi, O. Mashtalir, L. Pan, B. Zhang, J. Yang, Y. Gogotsi, S.J. Billinge, M.W. Barsoum, *Chem. Commun.* **50**, 9517 (2014)
71. A. Brady, K. Liang, V.Q. Vuong, R. Sacci, K. Prenger, M. Thompson, R. Matsumoto, P. Cummings, S. Irle, H.-W. Wang, *ACS Nano* **15**, 2994 (2021)
72. W. Sun, H.W. Wang, L. Vlcek, J. Peng, A.B. Brady, N.C. Osti, E. Mamontov, M. Tyagi, J. Nanda, S.G. Greenbaum, *Adv. Mater. Interfaces* **7**, 1902207 (2020)
73. J. Zhang, S. Seyedin, S. Qin, Z. Wang, S. Moradi, F. Yang, P.A. Lynch, W. Yang, J. Liu, X. Wang, *Small* **15**, 1804732 (2019)
74. P. Xue, H. Bisoyi, Y. Chen, H. Zeng, J. Yang, X. Yang, P. Lv, X. Zhang, A. Priimagi, L. Wang, *Angew. Chem. Int. Ed.* **60**, 3390 (2020)
75. K.A.S. Usman, J. Zhang, D.Y. Hegh, A.O. Rashed, D. Jiang, P.A. Lynch, P. Mota-Santiago, K.L. Jarvis, S. Qin, E.L. Prime, *Adv. Mater. Interfaces*, 2002043 (2021)
76. N.C. Osti, M. Naguib, A. Ostadhossein, Y. Xie, P.R. Kent, B. Dyatkin, G. Rother, W.T. Heller, A.C. Van Duin, Y. Gogotsi, *ACS Appl. Mater. Interfaces* **8**, 8859 (2016)
77. J. Hermans, P. Hermans, D. Vermaas, A. Weidinger, *Recl. Trav. Chim. Pays-Bas* **65**, 427 (1946)
78. H. Shao, K. Xu, Y.-C. Wu, A. Iadecola, L. Liu, H. Ma, L. Qu, E. Raymundo-Pinero, J. Zhu, Z. Lin, *ACS Energy Lett.* **5**, 2873 (2020)

79. M. Han, X. Yin, H. Wu, Z. Hou, C. Song, X. Li, L. Zhang, L. Cheng, *ACS Appl. Mater. Interfaces* **8**, 21011 (2016)
80. Y. Liu, Y. Jiang, Z. Hu, J. Peng, W. Lai, D. Wu, S. Zuo, J. Zhang, B. Chen, Z. Dai, *Adv. Funct. Mater.* **31**, 2008033 (2021)
81. C. Wang, S. Chen, L. Song, *Adv. Funct. Mater.* **30**, 2000869 (2020)
82. G.S. Henderson, F.M. De Groot, B.J. Moulton, *Rev. Min. Geochem.* **78**, 75 (2014)
83. C. Wang, S. Chen, H. Xie, S. Wei, C. Wu, L. Song, *Adv. Energy Mater.* **9**, 1802977 (2019)
84. A. Qian, Y. Pang, G. Wang, Y. Hao, Y. Liu, H. Shi, C.-H. Chung, Z. Du, F. Cheng, *ACS Appl. Mater. Interfaces* **12**, 54791 (2020)
85. A. Sarycheva, Y. Gogotsi, *Chem. Mater.* **32**, 3480 (2020)
86. R. Thakur, A. VahidMohammadi, J. Moncada, W.R. Adams, M. Chi, B. Tatarchuk, M. Beidaghi, C.A. Carrero, *Nanoscale* **11**, 10716 (2019)
87. O. Pecher, J. Carretero-González, K.J. Griffith, C.P. Grey, *Chem. Mater.* **29**, 213 (2017)
88. F. Blanc, M. Leskes, C.P. Grey, *Acc. Chem. Res.* **46**, 1952 (2013)
89. A. Kuhn, M. Kunze, P. Sreeraj, H.-D. Wiemhöfer, V. Thangadurai, M. Wilkening, P. Heitjans, *Solid State Nucl. Magn. Reson.* **42**, 2 (2012)
90. K.J. Griffith, M.A. Hope, P.J. Reeves, M. Anayee, Y. Gogotsi, C.P. Grey, *J. Am. Chem. Soc.* **142**, 18924 (2020)
91. S. Kajiyama, L. Szabova, K. Sodeyama, H. Iinuma, R. Morita, K. Gotoh, Y. Tateyama, M. Okubo, A. Yamada, *ACS Nano* **10**, 3334 (2016) □

Xuehang Wang is currently an assistant professor in the Department of Radiation Science and Technology at Delft University of Technology, The Netherlands. She received her PhD degree in chemical engineering from the Norwegian University of Science and Technology in 2016, and was a postdoctoral researcher at A.J. Drexel Nanomaterials Institute, Drexel University. Her research interests include the charge storage mechanism of energy storage devices, especially the electrolyte transportation at electrode-electrolyte interphases of two-dimensional MXenes and various carbon materials. Wang can be reached by email at x.wang-22@tudelft.nl.

Lars Bannenberg is currently an assistant professor in the Department of Radiation Science and Technology at Delft University of Technology, The Netherlands. He received his MSc in financial economics from Erasmus University Rotterdam in 2015, as well as MSc (2015) and PhD degrees (2019) in applied physics from Delft University of Technology. His research interests include thin film materials and interfaces of energy materials such as batteries and materials for optical hydrogen sensors. To study these materials, Bannenberg uses a wide variety of neutron- and x-ray scattering techniques. Currently, he is also responsible for the neutron reflectometer at the Reactor Institute Delft. Bannenberg can be reached by email at l.j.bannenberg@tudelft.nl.